Design of a Multifunctional Interlayer for NASCION-Based Solid-State Li Metal Batteries

(article starts on next page)

Design of a Multifunctional Interlayer for NASCION-Based Solid-State Li Metal Batteries

Shizhao Xiong,* Yangyang Liu, Piotr Jankowski, Qiao Liu, Florian Nitze, Kai Xie, Jiangxuan Song,* and Aleksandar Matic*

NASCION-type Li conductors have great potential to bring high capacity solid-state batteries to realization, related to its properties such as high ionic conductivity, stability under ambient conditions, wide electrochemical stability window, and inexpensive production. However, their chemical and thermal instability toward metallic lithium (Li) has severely hindered attempts to utilize Li as anode material in NASCION-based battery systems. In this work, it is shown how a tailored multifunctional interlayer between the solid electrolyte and Li anode can successfully address the interfacial issues. This interlayer is designed by creating a quasi-solid-state paste in which the functionalities of LAGP ($Li_{1.5}Al_{0.5}Ge_{1.5}(PO_4)_3$) nanoparticles and an ionic liquid (IL) electrolyte are combined. In a solid-sate cell, the LAGP-IL interlayer separates the Li metal from bulk LAGP and creates a chemically stable interface with low resistance (≈ 5 Ω cm^2) and efficiently prevents thermal runaway at elevated temperatures (300 °C). Solid-state cells designed with the interlayer can be operated at high current densities, 1 mA cm^{-2}, and enable high rate capability with high safety. Here developed strategy provides a generic path to design interlayers for solid-state Li metal batteries.

1. Introduction

Solid-state lithium batteries (SSLBs) are currently at focus as one of the most promising candidates for next generation battery technology. The interest arises from the possibility to use high-voltage cathodes and high-capacity lithium (Li) metal anodes without compromising the safety.[1] The safety concerns in commercial Li-ion batteries (LIBs) are tightly connected to the flammable organic liquid electrolytes that are currently used. Liquid electrolytes also have a limited electrochemical window and are often incompatible with the use of metallic Li as anode.[2,3] In SSLBs the liquid electrolyte is entirely replaced by a solid electrolyte enabling safe operation even under abuse conditions as well as compatibility with high-voltage cathodes (electrochemical stability window up to 6.0 V can be achieved[4]) and high-capacity Li metal anode paves the way for dramatically gravimetric and volumetric energy densities for the full cells.[5,6] In addition, SSLBs are expected to have prolonged cycle life because of the suppressed chemical "cross talk" between electrodes.[7]

Considerable efforts have been devoted to exploring various classes of solid electrolytes for Li metal batteries. They can generally be divided into inorganic/ceramic and organic polymer electrolytes. Owing to a considerably higher ionic conductivity at ambient temperature ($>10^{-3}$ S cm^{-1}), high Li-ion transference number (≈ 1) and high thermal stability, inorganic Li-ion conductors, such as LiSICON,[8] thio-LiSICON,[9] NASICON,[10] perovskites,[11] anti-perovskites,[12] garnet,[13] sulfide-type ceramic/glass,[14] and hydrides,[15] have been at focus. Among the broad variety of Li-ion conductors, NASICON type superionic conducting glass ceramics, like $Li_{1+x}Al_xGe_{2-x}(PO_4)_3$ (LAGP) and $Li_{1+x}Al_xTi_{2-x}(PO_4)_3$ (LATP), show great promise to meet the practical demands for SSLBs.[16,17] By optimizing the preparation procedure LAGP electrolytes can reach high conductivity of $>5 \times 10^{-3}$ S cm^{-1} at ambient conditions.[18] Moreover, LAGP electrolytes are generally very stable in normal atmosphere[19] and have a wide electrochemical stability window.[4] These feature, combined with relatively easy sintering process qualify LAGP electrolyte as a competitive candidate for commercial applications of SSLBs.[20]

Despite the above-mentioned merits, the integration of LAGP electrolyte in SSLBs is still hampered by the formation

Dr. S. Xiong, Y. Liu, Q. Liu, Prof. J. Song
State Key Laboratory for Mechanical Behavior of Materials
Xi'an Jiaotong University
Xi'an 710049, P. R. China
E-mail: songjx@xjtu.edu.cn
Dr. S. Xiong, Dr. F. Nitze, Prof. A. Matic
Department of Physics
Chalmers University of Technology
Göteborg SE 41296, Sweden
E-mail: shizhao.xiong@chalmers.se; matic@chalmers.se
Dr. P. Jankowski
Department of Energy Conversion and Storage
Technical University of Denmark
Kgs. Lyngby 2800, Denmark
Prof. K. Xie
College of Aerospace Science and Engineering
National University of Defense Technology
Changsha, Hunan 410073, P. R. China

The ORCID identification number(s) for the author(s) of this article can be found under https://doi.org/10.1002/adfm.202001444.

ADVANCED
SCIENCE NEWS
www.advancedsciencenews.com

ADVANCED
FUNCTIONAL
MATERIALS
www.afm-journal.de

of a chemically unstable interface when it is coupled with a Li metal anode. Firstly, instability of LAGP toward metallic Li results in series of degradation reactions at the Li/electrolyte interface at physical contact.[21] The reaction products form an interphase with a considerable electronic conductivity but decreased ionic conductivity compared to the bulk solid electrolyte. This interphase acts as a role of solid electrolyte interphase (SEI) layer in commercial LIBs, thus named mixed conducting interphase (MCI).[22] The growth of the interphase leads to a constantly increasing interfacial resistance and a volume change, even fracture of bulk electrolyte, upon cycling.[23] In addition, there is a potential risk for a strong thermal runaway since the components of the interphase release of oxygen gas at relatively high temperatures (>200 °C).[24] Thus, stabilization of the interface between the LAGP electrolyte and metallic Li anode is a key issue for high capacity SSLBs without a rapid performance degradation and underlying safety issues.

The design of an interlayer on LAGP electrolyte is considered as an effective approach to address the reactivity at the interface between the solid electrolyte and Li metal.[21,24] Recently, considerable progress on building interlayers for LAGP based SSLBs have been reported, such as Germanium (Ge) thin film coating,[25] three-dimensional polymer-gel layers,[26] lithium phosphorous oxynitride (LiPON) layers,[27] or conductive poly(oxyethylene) (PEO) layers.[28] Nevertheless, the interfacial resistances reported are still too high and thus the areal current density applied in these studies is usually in the range of 0.1–0.3 mA cm^{-2}, which is far from the practical demands for SSLBs when using high capacity cathode materials, and using high active material loading, and high discharge/charge rates.[21] Moreover, a potential hazard of thermal runaway at relatively high temperatures (>200 °C) for LAGP based SSLBs has rarely been considered or estimated by the reported strategies. It is worth emphasizing that high safety is one of primary motives to explore and develop SSLBs.

In this work, we report on a multifunctional interlayer between LAGP electrolyte and Li metal anode which is designed as a hybrid paste formed by ball milling of LAGP nanoparticles and a room temperature ionic liquid (IL). The functionality of the interlayer stems from the high ionic conductivity of both components and the formation of a chemically stable interphase on the Li metal anode by controlled breakdown of the IL (N-Methyl-(n-butyl) imidazolium bis(fluorosulfonyl)imide, BMIM-FSI). Thus, the LAGP-IL interlayer, which is of ultrahigh thermal stability and non-inflammability, is able to physically separate the bulk LAGP electrolyte and Li metal avoiding the formation of an MCI and eventually suppressing the degradation reactions as well as thermal runaway. This interlayer significantly lowers the interfacial resistance and allows the use of a high areal current density, 1.0 mA cm^{-2}, at ambient temperature, which is roughly an order of magnitude higher than previously reported (0.1–0.3 mA cm^{-2}).[21]
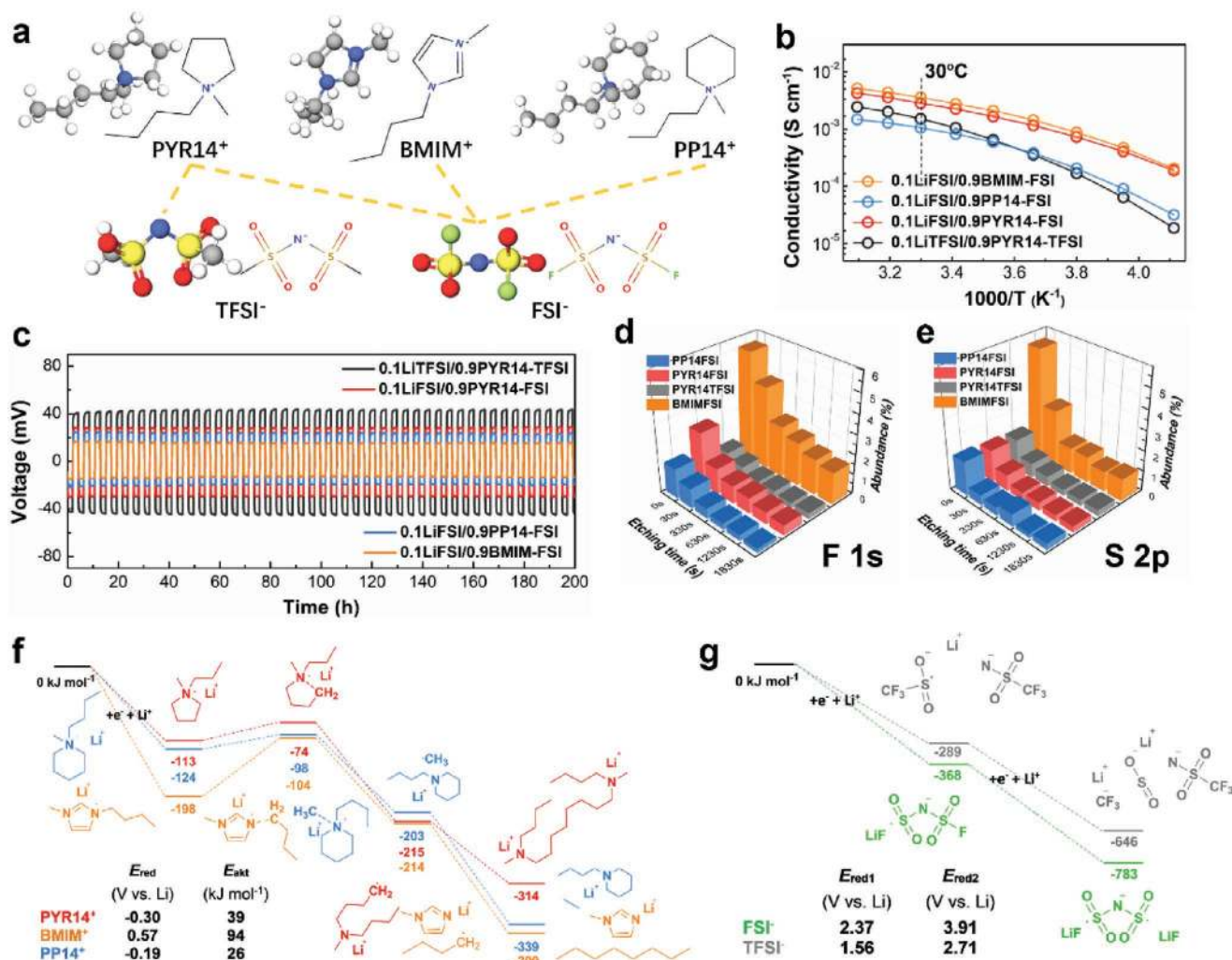
2. Results and Discussion

2.1. Selection of Ionic Liquid Electrolyte

To prepare a stable hybrid interlayer we have screened ILs previously showing good performance in Li-battery applications.[29–32] These are based on three cations, 1-butyl-1-methylpyrrolidinium (PYR14$^+$), 1-butyl-1-methylpiperidinium (PP14$^+$) and 1-butyl-3-methylimidazolium (BMIM$^+$), and two anions, bis(trifluoromethanesulfonyl)imide (TFSI$^-$) and bis(fluorosulfonyl)imide (FSI$^-$), combined in four ILs named PYR14-TFSI, PYR14-FSI, BMIM-FSI and PP14-FSI. The chemical structures of cations and anions are shown in **Figure 1**a. To form IL based electrolytes, Li salts with the same anion as in corresponding IL was also added. All IL based electrolytes show a high room temperature conductivity with the BMIM-FSI based electrolyte (0.1LiFSI/0.9BMIM-FSI) having the highest one of 3.6 mS cm^{-1} at 30 °C, as plotted in Figure 1b. To evaluate the compatibility of IL electrolytes toward a Li metal electrode, galvanostatic cycling and electrochemical impedance spectroscopy (EIS) experiments on Li-Li symmetric cells were performed (Figure 1c and Figure S1, Supporting Information). The overpotential profiles, as seen in Figure 1c, show stable cycling with all IL electrolytes over 200 h at a low current density of 0.1 mA cm^{-2} which is generally used to run solid state batteries.[21] It is worth noting that the cell with 0.1LiFSI/0.9BMIM-FSI holds the lowest overpotential of ≈16 mV in the comparison of a variety of IL electrolytes. The results of EIS shown in Figure S1 (Supporting Information) reveal that the SEI layers formed with FSI$^-$ based IL electrolytes have a much lower resistance to Li$^+$ transport compared to that formed in the presence of the TFSI anion.

To further reveal the mechanism behind the stability of IL-electrolytes and the nature of the interphase, X-ray photoelectron spectroscopy (XPS) analysis was performed on Li electrodes retrieved from cycled symmetric cells. The F 1s spectra (Figure S2, Supporting Information) from the Li surface before argon ion sputtering indicates that the main breakdown product in electrolytes with FSI$^-$ is LiF (≈685.0 eV) while in TFSI$^-$ based electrolytes more C–F species (≈689.0 eV) are found compared to LiF, which is consistent with previous publications.[33–35] Depth profiling reveals that the decomposition products are present throughout the SEI layer formed with IL electrolytes, as shown in Figure 1d,e and Figure S2 (Supporting Information). In particular, the SEI layer on the Li metal anode cycled with 0.1LiFSI/0.9BMIM-FSI has a higher concentration of LiF compared to the layers formed with the other electrolytes. The higher concentration of LiF is beneficial for stabilizing the electrodeposition of Li during the plating and stripping reactions since the presence of lithium halide salts enhances the surface mobility of Li.[36]

To obtain a better understanding about the decomposition process of ILs on Li metal, DFT modeling was performed. For the cations (PYR14$^+$, BIMIM$^+$, PP14$^+$), breakdown of various bonds was investigated (Figures S3–S6, Supporting Information) to determine the most probable reduction process for each cation and the diagrams following the lowest energy barrier are shown in Figure 1f,g. The reduction of cations is expected to be slowed down by kinetic barriers with an activation energy E_{akt} which is needed to be overcome during the decomposition process. In addition, reduction potentials (E_{red}) for cations were calculated by thermodynamic cycle. The reduction of BMIM$^+$ shows higher value of E_{red} but also the highest activation energy, resulting in expected kinetic stability. As a result of that the reduced form of BMIM, with longer lifetime, can diffuse from the electrode and transfer an electron to the anion enhancing FSI decomposition. In the case of PYR14$^+$ and PP14$^+$, E_{red} is below 0 V versus Li, which indicates their stability against Li.

**ADVANCED
SCIENCE NEWS**

www.advancedsciencenews.com

**ADVANCED
FUNCTIONAL
MATERIALS**

www.afm-journal.de

Figure 1. Interfacial stability of ionic liquids on Li metal electrodes. a) Chemical structures of cations and anions of investigated ionic liquids. b) Ionic conductivity as a function of temperature for the ionic liquid electrolytes. c) Cycling stability of Li|IL electrolyte symmetric cells with different ionic liquid electrolytes at current density of 0.1 mA cm^{-2}. d,e) Depth profile of fluorine at the Li metal surface, obtained from XPS experiments with different argon ion sputtering time, after cycling with ionic liquid electrolytes. f,g) Energy diagrams for most favorable reduction pathways of the ionic liquids.

However, slow reduction and decomposition can be possible at higher potentials, and would not be kinetically blocked due to a low energy barrier.[37] Much faster and easier reduction is predicted for both of anions, there is no energy barrier for breakdown of both FSI$^-$ and TFSI$^-$ (Figure 1f and Figures S7 and S8, Supporting Information). This suggests that anion decomposition mostly contributes to SEI formation, with FSI$^-$ more prone to reduction by Li. The decomposition of TFSI$^-$ is a step-by-step process toward smaller species while an immediate formation of LiF is suggested for the reduction mechanism of FSI$^-$, in agreement with previous studies.[38] On account of its high ionic conductivity and the formation of an SEI layer with fast Li-ion migration (high concentration of LiF) and high stability and low overpotential of the Li metal electrode during stripping and plating, 0.1LiFSI/0.9BMIM-FSI is chosen as the liquid component to design a highly conductive and stable interlayer between bulk LAGP and Li metal.

2.2. Preparation of LAGP-IL Hybrid Paste

In general, a certain external pressure is applied to Li batteries to maintain good contact between the components during cycling, in particular to SSLBs.[39] For cells with a liquid component this pressure will squeeze out the liquid (in our work an ionic liquid electrolyte) if it is solely placed between a solid-state electrolyte (e.g., LAGP) pellet and Li metal electrode. Mixtures of ILs with nanoparticles, such as fumed silica, has been reported to form quasi-solid-state nanocomposite ion gels.[40] Here we chose to mix LAGP nanoparticles with 0.1LiFSI/0.9BMIM-FSI to form a gel-like hybrid paste (**Figure 2**a), with considerable retention of the liquid component under external pressure, following previous reports that have demonstrated that the addition of LAGP particles in hybrid electrolytes is beneficial for enhancing Li-ion migration.[41] The LAGP nanoparticles, with an average radius of 100 nm, are obtained by multiple ball-milling
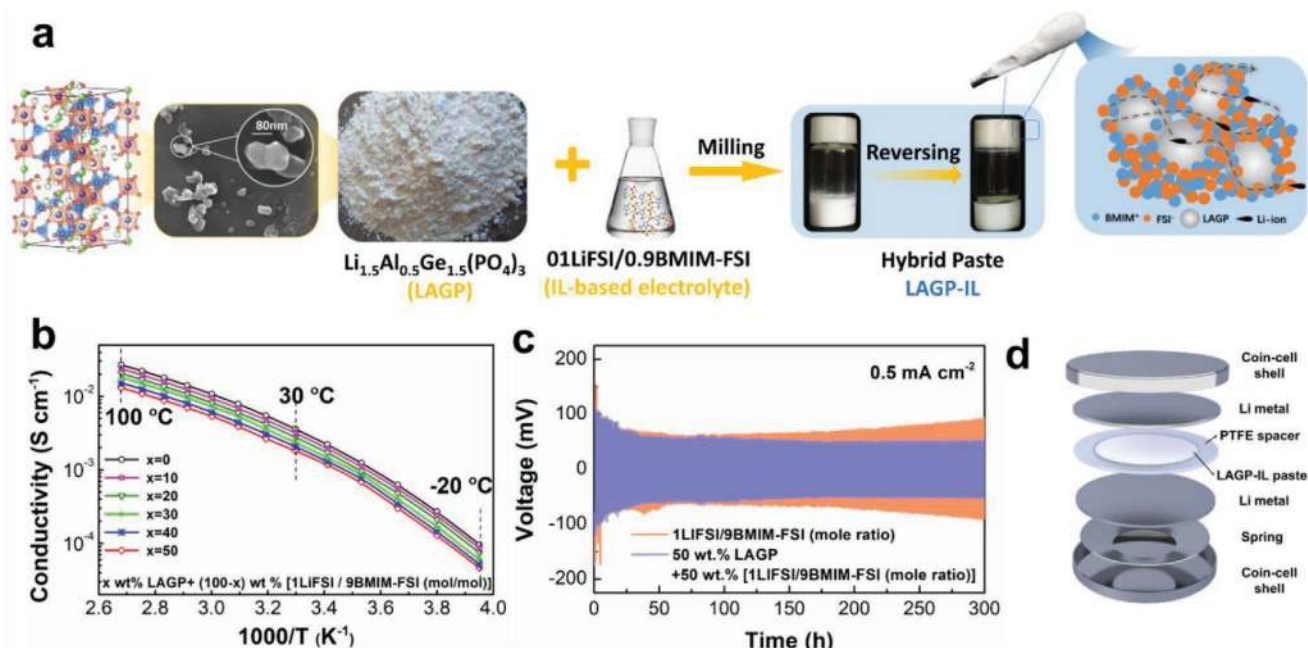
Figure 2. Preparation of LAGP-IL hybrid paste and corresponding electrochemical performance. a) Schematic diagram of preparation of LAGP-IL hybrid paste (the mass fraction of LAGP nanoparticles is 50%). b) Ionic conductivity as a function of temperature for LAGP-IL hybrid paste for different LAGP mass fractions. c) Cyclic stability of Li–Li symmetric cells (configuration is shown in d) with LAGP-IL hybrid paste at a current density of 0.5 mA cm^{-2}.

(Figure S9, Supporting Information) and are also mixed with 0.1LiFSI/0.9BMIM-FSI by ball milling to prepare a series of hybrid pastes with different IL/nanoparticle ratios. When the mass fraction of LAGP nanoparticles is above 50% the paste does not flow for more than 24 h in a sample tube inversion test, thus showing a strong gelation.

The ionic conductivities as a function of temperature for the LAGP-IL hybrid pastes are shown in Figure 2b. The ionic conductivity decreases slightly with increased mass fraction of LAGP, but still remains above 10^{-3} S cm^{-1} at 30 °C for 50 wt% LAGP in the ionic liquid (Figure S10, Supporting Information). To reliably investigate the kinetics on the interface between LAGP and IL, a four-electrodes cell (Figure S11, Supporting Information) was used in EIS measurement. The derived activation energies for this interface is around 57 kJ mol^{-1}, which is comparable to previously reported results.[42,43] To evaluate the compatibility of the LAGP-IL hybrid paste on Li metal electrode galvanostatic cycling in Li–Li symmetric cells was performed (Figure 2c). The overpotential of the cell with neat IL electrolyte gradually increases after 200 h, indicating an unstable interface on Li electrode under a relatively high current density of 0.5 mA cm^{-2}. In contrast, the cell with LAGP-IL hybrid paste shows stable cycling for more than 300 h, which is generally attributed to the formation of a robust SEI layer on Li.

2.3. Thermal Evaluation of LAGP-IL Interlayer

To evaluate the thermal stability the LAGP-IL interlayer, we performed the similar procedure as reported previously.[24] The heating process for two systems is shown in Video S1 (Supporting Information) (LAGP pellet in direct contact with Li)

and Video S2 (Supporting Information) (LAGP-IL interlayer between LAGP pellet and Li). **Figure 3**a shows successive images as a function of time for the LAGP pellet in contact with molten Li. As previously reported,[24] three stages were observed for the behavior of the LAGP pellet on molten Li. Initially it is floating on the surface (00:00 to 03:00), followed by cracking LAGP (03:30 to 03:50) and finally showing a severe thermal runway with a super-bright flash (04:00), causing both the LAGP pellet and the Li to burn to ash (Figure 3c–i). It is worth noting that the reaction generated enough heat to melt the case of the coin cell (Figure 3c–ii) which is made of stainless steel (melting point ≈1400 °C[44]). This heat, which is completely generated inside the cell, would be fatal for all commercial packaging materials for batteries. Thus, the thermal runway of LAGP based SSLBs needs to be addressed to bring it to practical application. The LAGP pellet covered by LAGP-IL interlayer also floated on the molten Li at the beginning but slowly sank (as seen in Figure 2b), showing good wettability by Li metal as compared with the bulk solid electrolyte pellet. However, no strong thermal reaction occurs even during an extended heating time of 40 min. After the heating process, no damage is found on the coin cell case (Figure 3c–iv) but a large amount of black reaction product accumulates around the LAGP pellet (Figure 3c–iii). The intact LAGP pellet in fact is still functional as shown by the performance of a recovered pellet (Figure 3c–vi) that is washed in ethanol (Figure 3c–vii) and put in a Li–Li symmetric cell. This cell exhibits stable cycling for 200 h at a current density of 0.1 mA cm^{-2} (Figure S12, Supporting Information).

To elucidate the mechanism behind the ability of the interlayer to suppress thermal runaway, the LAGP-IL paste was heated in contact with Li metal, following the same procedure
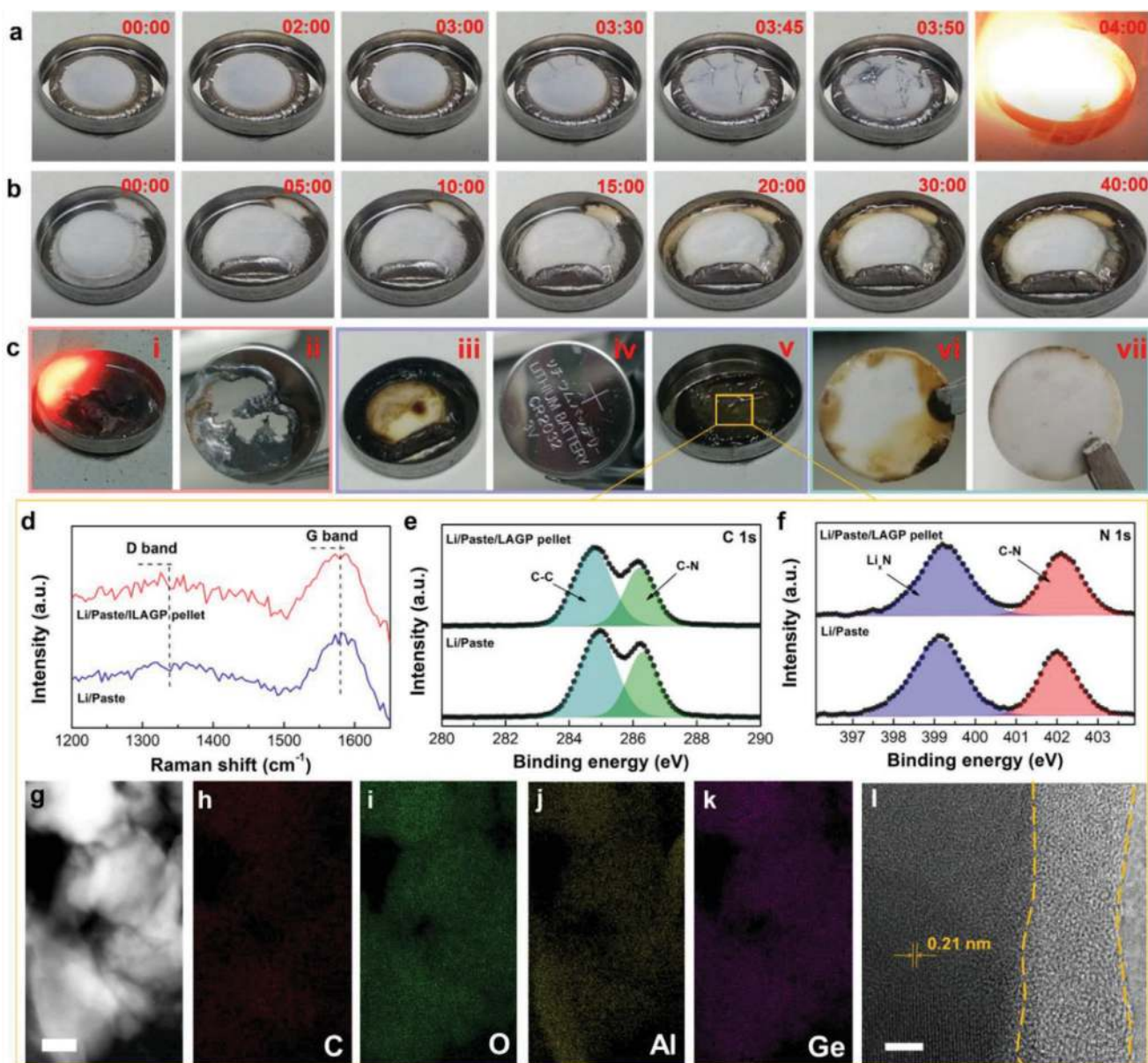
Figure 3. Evaluation of the thermal stability of LAGP/Li interfaces. a,b) Successive images of a LAGP pellet in contact with Li metal without (a) and with (b) the LAGP-IL interlayer as a function of time (in minutes and seconds) at 300 °C. Thermal tests were carried out in argon glove box (oxygen and water were both below 0.1 ppm). c) Optical images of end products after thermal test without (i,ii) and with (iii–vii) LAGP-IL interlayer. d) Raman spectra and e,f) XPS spectra of C 1s and N 1s for the products on the Li for the two tests (Li/hybrid paste and Li/hybrid paste/LAGP pellet). g–l) High-resolution transmission electron microscopy (HRTEM) image of the products (g,l) and corresponding mapping of C (h), O (i), Al (j), and Ge (k). Scale bars, 100 nm (g–k), 5 nm (l).

as previously conducted (Figure S13, Supporting Information). The similar black products were observed and characterized by using Raman spectroscopy, XPS and high-resolution transmission electron microscopy (HRTEM). The morphology of heated Li electrode shows bulk pieces of reaction products mainly consisting of C, O and Ge, as seen in Figure S14 (Supporting Information). The elements are further verified by XPS (Figure S14c, Supporting Information). High resolution XPS spectra of C 1s display two peaks at 284.8 and 286.3 eV which are corresponding to C–C and C–N groups, respectively (Figure 3d) and in N 1s spectra, a signature of Li_xN species at 399.2 eV and

C–N groups at 402.1 eV are detected (Figure 3e). These results indicate that the reaction products can be attributed to the decomposition of ionic liquid cation and anion. From Raman scattering we can also conclude that amorphous carbon is generated in the heating process by the presence of the G band (1580 cm^{-1}) observed in Raman spectra[45] and Raman mapping of the G band shows that the amorphous carbon distributed over the products emerged out of the reaction between molten Li and d LAGP-IL hybrid paste (Figure S15, Supporting Information). HRTEM images (Figure 3g–k) show that the LAGP and carbon are integrated in the end products. Figure 3l shows

**ADVANCED
SCIENCE NEWS**

www.advancedsciencenews.com

**ADVANCED
FUNCTIONAL
MATERIALS**

www.afm-journal.de

that the LAGP nanoparticles are coated by amorphous carbon and that their high-degree crystallinity is preserved during the heating process, as a result of effective insulation by the carbon layer. This carbon layer guarantees the stability of LAG-IL interlayer by which the LAGP pellet and molten Li are entirely separated during the heating process, avoiding the potential risk of thermal runaway in LAGP based SSLBs.

2.4. Interfacial Stability with LAGP-IL

To evaluate the stability of interface during electrochemical process, Li|LAGP pellet|Li symmetric cells were assembled with the LAGP-IL interlayer (as shown in Figure S16, Supporting Information) or with a liquid electrolyte (LE) to wet the interface, for comparison. The voltage profiles of symmetric cells during galvanostatic cycling are shown in **Figure 4**a. An increase in overpotential is evident for the cell with the interface wetted by LE. This increase is generally associated with the formation and

growth of a SEI layer on the Li metal electrode and accumulation of dead Li at the interface.[46] After 750 h a sudden drop of the voltage indicates an internal short circuit as a result of the penetration of dendrites, caused by local Li plating at defects, through the solid electrolyte.[47] The symmetric cell without interlayer or LE wetting shows even poorer cyclic stability, as seen in Figure S17 (Supporting Information). In contrast, the cell with the LAGP-IL interlayer exhibits a low and steady overvoltage of 30 mV for 1500 h, showing that this configuration has an outstanding long-term cycling stability and a low interfacial resistance.

The evolution of degradation reactions on the interfaces was further investigated by XPS and EIS. The Ge 3d spectra of the pristine LAGP pellet shows a distinct peak at 32.5 eV (Figure 4b), corresponding to the Ge^{4+} oxidation state in the solid electrolyte. In the spectra for LAGP pellet cycled with LE wetting the interface, a second peak appears in the Ge 3d spectrum at the binding energy of elemental Ge (29.0 eV), demonstrating that Ge^{4+} on the surface of LAGP was partly reduced to
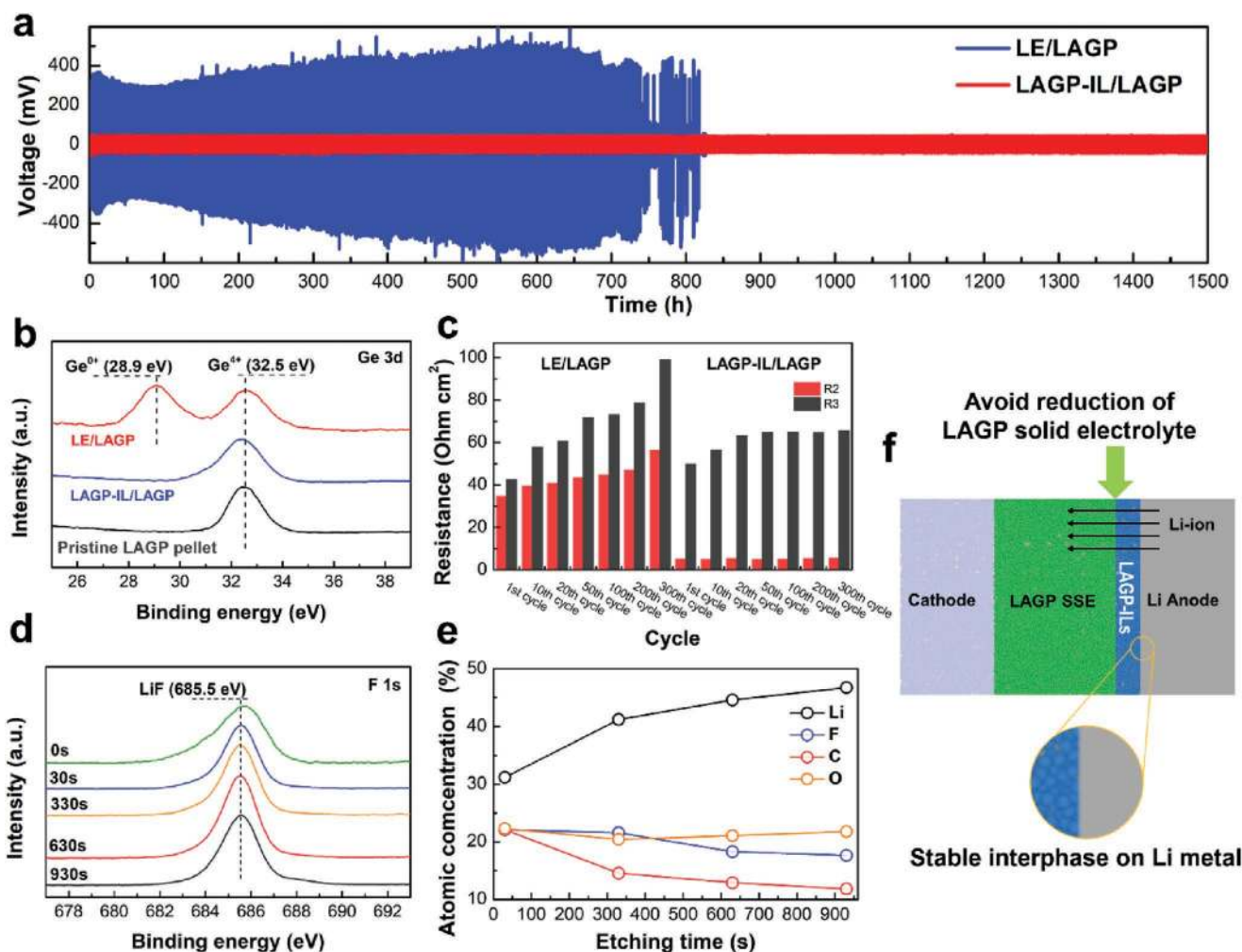

Figure 4. Interfacial stability of bulk LAGP pellet and Li anode. a) Voltage profiles of Li|LAGP pellet|Li symmetric cells with a LAGP-IL interlayer or a liquid electrolyte (LE, 1 M $LiPF_6$ in EC/DEC) to wet the interface, operating at a current density of 0.1 mA cm^{-2} and a capacity density of 0.1 mAh cm^{-2}. b,c) XPS spectra of Ge 3d (b) from the interface of the LAGP pellets and interfacial impedance (c) in the cycled cells with the LAGP-IL interlayer or the LE at the interface. d) XPS F 1s spectra of the Li anode cycled with the LAGP-IL interlayer. e) Elemental composition of the SEI layer on retrieved Li anodes cycled with the LAGP-IL interlayer. f) Schematic diagram of the role of LAGP-IL interlayer between bulk electrolyte and Li.

**ADVANCED
SCIENCE NEWS**
www.advancedsciencenews.com

**ADVANCED
FUNCTIONAL
MATERIALS**
www.afm-journal.de

form an MCI, in agreement with previous suggestions.[22] For the LAGP pellet cycled with the LAGP-IL interlayer a reduction of Ge^{4+} on the surface cannot be observed. EIS spectra of the symmetric cells after different numbers of cycles are shown in Figure S18 (Supporting Information). In the figure, R2 and R3 represent the resistances for Li-ion migration through the SEI layer and through the interface between the interlayer and LAGP pellet, respectively.[43] The R2 and R3 values of the cell using LE to wet the interface show a slow increase with increased number of cycles, which can be attributed to the accumulation of degradation products at the interface. When using the LAGP-IL interlayer a low value of R2 ($\approx 5 \ \Omega \ cm^2$) indicates that a highly conductive SEI layer on Li metal electrode is formed. This SEI layer is found to be stable during repeated electrochemical plating and stripping of Li. XPS spectra and the elemental composition of the SEI as a function of etching time (depth profiling) of this Li metal electrode are shown in Figure 4d,e. The results confirm that the breakdown of BMIM-FSI generates a significant amount of LiF (685 eV) throughout the SEI layer. Thus, the use of the LAGP-IL interlayer in solid state electrolyte cell not only stops the reduction of LAGP in the solid electrolyte but also contributes to the formation of a highly conductive and stable SEI layer on Li metal electrode (Figure 4f).

From optical images a massive amount of black dead Li was found for the retrieved Li metal anodes with LE wetting the interface while Li metal anodes cycled using the LAGP-IL interlayer exhibits a smooth surface, as seen in Figure S19 (Supporting Information). On shorter length scales SEM images (Figure S20, Supporting Information) confirm the presence of cracks and large accumulation of dead Li on the surface when the LE was used to wet the interface. In cross sectional SEM images, a porous structure created by the side reaction between Li and LE is revealed, which will lead to consumption or even drying out of the LE. This result is consistent with the electrochemical behavior shown in Figure 4. It is worth noting that the growth of Li dendrites is observed on the Li metal electrode cycled in 0.1LiFSI/0.9BMIM-FSI IL electrolyte despite its high chemical stability toward metallic Li (Figure S21, Supporting Information). This suggests that a nonuniform Li-ion flux on the surface of Li invariably induces localized plating.[48] Nevertheless, the SEM images in **Figure 5** provide clear evidence that the growth of Li dendrites is effectively suppressed by using the LAGP-IL interlayer. This result is fully in line with previous reports pointing toward the potential of ion conducting nanoparticles distributed on a Li metal surface to regulate Li-ion flux and uniform plating for a dendrite-free Li anode.[48]

2.5. SSLBs with LAGP-IL Interlayer

The electrochemical performance of the LAGP-IL interlayer is systemically evaluated in symmetric and full cells. To determine the critical current density galvanostatic cycling of the symmetric cells at step-wise increasing current densities, from 0.05 to 2.0 mA cm^{-2}, was performed (**Figure 6**a). For the cell with LE wetting the interface, the voltage initially increased with increasing current but suddenly drop at 0.4 mA cm^{-2}, which is defined as the critical current density for this configuraiton.[49]
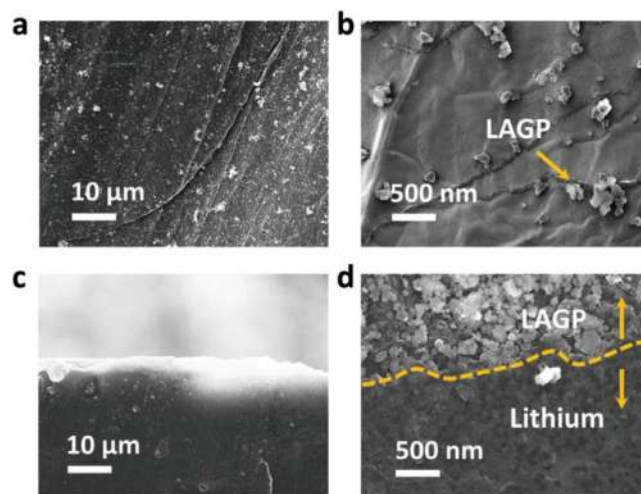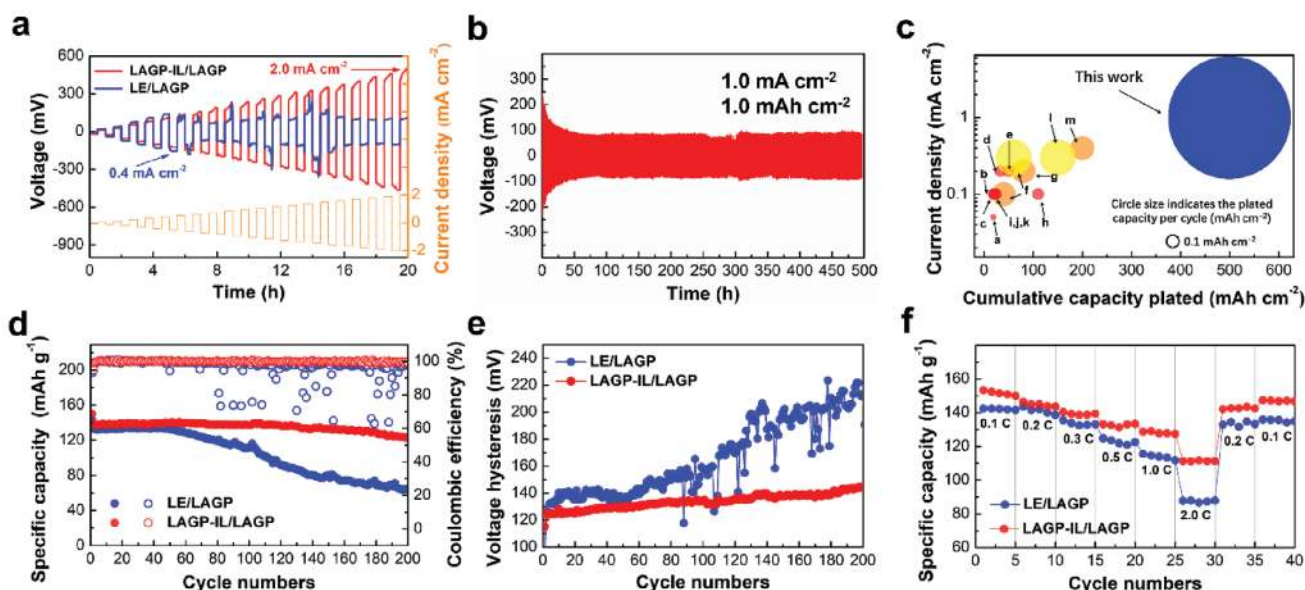

Figure 5. Morphology of cycled Li metal anodes. a,b) Top view SEM images of cycled Li anode with LAGP-IL interlayer in low-magnification (a) and high-magnification (b). c,d) Cross sectional SEM images in low-magnification (c) and high-magnification (d). All Li metal anodes are retrieved from symmetric cells after 200 cycles at a current density of 0.1 mA cm^{-2}.

With the LAGP-IL interlayer in the cell stable stripping/plating is observed even at a high current density, up to 2.0 mA cm^{-2}. The symmetric cell with LAGP-IL interlayer was also investigated with respect to long-term cycling stability at high current density, 1.0 mA cm^{-2}, (Figure 6b), and was showed stable cycling for more than 500 h. As previously reported, the current density, capacity density per cycle and cumulative capacity of plated Li are regarded as significant parameters for practical utilization of Li metal anodes in SSLBs. The comparison of the parameters in our work with those of recent literatures (plots a-m) that use NASICON type solid electrolytes to build SSLBs is summarized in Figure 6c. Previous results in literature for cells with LAGP electrolyte and Li metal anode can only sustain low current densities (generally around 0.1 mA cm^{-2}) and insufficient accumulative capacity density (less than 200 mAh cm^{-2}), due to the poor interfacial stability and high resistance at the SSE/Li interface, far from the practical demands. This limitation is overcome by our design of the LAGP-IL interlayer that enables cycling with current densities one order of magnitude higher than previously reported and a more than doubled accumulative capacity (500 mAh cm^{-2}). Moreover, as shown in Table S1 (Supporting Information), the cell with the LAGP-IL interlayer in our work shows higher interfacial stability compared with the results in previous reports using oxide solid electrolytes and is even comparable to those using sulfide or polymer solid electrolytes at room temperature.

Full cells were assembled by coupling the Li metal anode and LAGP solid electrolyte with a LiFePO$_4$ (LFP) cathode. The LAGP-IL interlayer was sandwiched between the LAGP pellet and the LFP cathode as well as between the LAGP pellet and the Li metal anode. Due to the higher electrochemical stability window, 1LiFSI/9PYR14-FSI electrolyte used in the interlayer on the LFP cathode side, instead of 1LiFSI/9BMIM-FSI. As shown in Figure 6d, the full cell with LAGP-IL interlayer exhibits outstanding cycling stability with a capacity fading of

**ADVANCED
SCIENCE NEWS**
www.advancedsciencenews.com

**ADVANCED
FUNCTIONAL
MATERIALS**
www.afm-journal.de

Figure 6. Electrochemical performance of SSLBs with LAGP-IL interlayer at room temperature. a) Galvanostatic cycling of Li|LAGP pellet|Li symmetric cells at increased current densities, from 0.05 to 2.0 mA cm^{-2}. b) Voltage profiles of symmetric cells with LAGP-IL interlayer operated at a high current density, 1.0 mA cm^{-2}, and a high capacity density of 1.0 mAh cm^{-2}. c) Comparison of cycling performance of symmetric cell with LAGP-IL interlayer with that of recent publications[23,25–28,50–57] (a-ref. [50], b-ref. [51], c-ref. [25], d-ref. [52], e-ref. [53], f-ref. [54], g-ref. [55], h-ref. [28], i-ref. [26], j-ref. [27], k-ref. [23], l-ref. [56], m-ref. [57]). d–f) Cyclic performance (d), corresponding polarization voltage (e) and rate performance of solid-state Li|LAGP |LiFePO$_4$ full cells with and without LAGP-IL interlayer. The rate in (d) and (e) was 0.3C. All the experiments were carried out at room temperature.

only 0.053% per cycle for 200 cycles. By contrast, the capacity of the full cell with a LE wetting the interface fades dramatically after 50 cycles, losing 51.8% capacity within 200 cycles. The stability of the cell with LAGP-IL interlayer is also shown by the voltage profiles (Figure S22, Supporting Information) and the evolution of voltage hysteresis (Figure 6e) which displays a slow increase without fluctuation, resulting from the stable interface and very low accumulation of inert by-products on the Li metal anode. The control cell instead shows a fast increase of voltage hysteresis, indicating the rapidly rising interfacial resistance. In addition, the rate capability is also enhanced with the LAGP-IL interlayer with a specific capacity of >110 mAh g^{-1} at 2C as shown in Figure 6f and Figure S23 (Supporting Information), respectively.

3. Conclusion

In summary, we report on a multifunctional interlayer to create a highly ion conducting, thermally and electrochemically stable interface between a LAGP solid electrolyte and Li metal anode for solid state Li batteries. The interlayer is based on the blend of an ionic liquid electrolyte and LAGP nanoparticles, forming a quasi-solid hybrid paste that easily can be applied in a cell with good mechanical and interfacial properties. The ionic liquid electrolyte component, 0.1LiFSI/0.9BMIM-FSI, ensures fast Li-ion transport and stability toward metallic Li. We show that this interlayer, placed between Li metal anode and LAGP pellet, efficiently suppresses the severe thermal runaway normally found for LAGP electrolyte at high temperatures. The carbonization of ionic liquid component generates an in-situ coating of amorphous carbon on the LAGP nanoparticles in the

interlayer that grants a thermal stability ensuring the separation of the bulk LAGP solid electrolyte and Li metal anode. The efficient separation of bulk LAGP pellet and Li metal prevents reduction of Ge^{4+} on the surface of solid electrolyte and suppresses the growth of Li dendrites by regulating Li-ion flux. With this interlayer, we realized ultra-stable cycling of Li|LAGP pellet|Li symmetric cells at a high current density and full Li|LAGP pellet|LiFePO$_4$ cells with high capacity at high rate and with very low fading (0.053% per cycle for 200 cycles). The introduction of ionic liquid in the cell design may lead to a slight increase in materials cost of the battery, but is justified by the advanced performance enabled by LAGP-IL interlayer. Moreover, the price of ionic liquids is expected to decrease as they are introduced in commercial production of batteries. Our results show a new route that can be explored for the practical application of LAGP based solid-state Li metal batteries.

4. Experimental Section

Preparation of LAGP Powder: The starting materials for Li$_{1.5}$Al$_{0.5}$Ge$_{1.5}$(PO$_4$)$_3$ (LAGP) synthesis were lithium carbonate (Li$_2$CO$_3$, Sigma-Aldrich, 99.99% purity), aluminum oxide (Al$_2$O$_3$, Sigma-Aldrich, 99.5% purity), Germanium dioxide (GeO$_2$, Sigma-Aldrich, >99.99% purity) and ammonium dihydrogen phosphate ((NH$_4$)$_2$PO$_4$, Sigma-Aldrich, ≥99.5% purity). They were stoichiometrically weighed and mixed by ball milling with 10 mm zirconia balls at 200 rpm for 4 h. The mixture was placed into a platinum pot and heated at a reaction temperature of 1350 °C for 2 h in a furnace to form the LAGP phase. Consequently, the pot was sharply cooled to room temperature and shifted to another furnace at 500 °C for 2 h for annealing. The bulk LAGP was ground with 10 mm zirconia balls in a zirconia container at 580 rpm for 6 h as dry milling to obtain the powder. After that, the LAGP powder was reground with 1 mm zirconia balls and ethanol solvent in a zirconia container at

580 rpm for 4 h as wet milling. 200 mg as-prepared LAGP powder was put into die and isostatic pressed into pellet, following by annealed at 850 °C for 6 h in muffle furnace.

Preparation of LAGP-IL Hybrid Paste: Lithium bis(fluorosulfonyl) imide (LiFSI, 99.95%, Sigma-Aldrich), N-Methyl-(n-butyl) imidazolium bis(fluorosulfonyl)imide (BMIM-FSI, 99.9%, Solvionic, water content is 20 ppm, analyzed by Karl Fischer titration) and as-prepared LAGP powder were used to prepare LAGP-IL hybrid paste. Firstly, the ionic liquid electrolyte was prepared by stirring the mixture of BMIM-FSI and LiFSI. The mixture of ionic liquid electrolyte and LAGP powder were sealed into a zirconia pot under argon atmosphere and ground (200 rpm for 30 min) to prepare the hybrid paste. The hybrid paste was collected in the glovebox after grinding to build the interlayer.

Characterization: The ionic conductivity of the electrolytes was measured on a Novocontrol broadband dielectric spectrometer in the temperature range from −20 to 100 °C in a gold-plated cell with Teflon spacer. The ESCALAB Xi+ X-ray photoelectron spectroscopy (XPS) was conducted to analysis chemical components on the surface of samples. Both the LAGP pellet and Li metal samples were washed by dimethyl ether (DME) after separation of the cell components. Lithium samples were transferred from glovebox to the chamber in a vessel without explosion in air. The area analyzed by the beam of in the XPS experiment was ≈400 µm in diameter. The diameter of LAGP particles was determined by a Zeta potential analyzer (ZetaPALS, Brookhaven) and the structure was determined by XRD-6100 powder X-ray diffraction Cu Kα radiation. SEM analysis was performed with a Leo Ultra 55 FEG SEM system. Raman spectra were observed from a Bruker IFS66 Fourier Transform spectrometer with a FRA106 Raman module. All the heating tests were carried out in Ar-filled glove box (both content of oxygen and water are below 0.1 ppm).

Preparation of LiFePO$_4$ (LFP) Cathode: LFP powder, super-P and polyvinylidene fluoride (PVDF) were dispersed into 1-Methyl-2-pyrrolidinone (NMP) in weight ratio of 8:1:1, following ball milling process to make uniform slurry. The LFP slurry was cast onto aluminum (Al) foil and dried at 100 °C for 24 h in vacuum oven. The mass loading of cathode is 5 mg cm^{-2}. LFP cathode was pouched into disks with diameter of 12 mm for assembling coin cells.

Coin Cell Fabrication and Electrochemical Test: Coin cells were assembled in glove box using CR2032 type shells. The symmetrical cells with LAGP-IL hybrid paste in Figure 2 were fabricated with two Li disks (thickness of 200 µm, China Energy Lithium Co., Ltd.) and a donut spacer (thickness of 25 µm). LAGP-IL hybrid paste was placed in the middle of spacer. The symmetrical cells with LAGP pellet in Figures 4 and Figure 6 were assembled with two Li disks and LAGP pellet. The interlayer was built with 5 µL commercial LE (1 M LiPF$_6$ in ethylene carbonate/diethyl carbonate mixture solvent) or 8 mg LAGP-IL paste hybrid on each side of LAGP pellet. The Li|LFP full cells were assembled with Li disk, LAGP pellet and LFP cathode. The interlayer in full cells was built in the same way for symmetric cells. The Li|LFP full cells were operated at rate of 0.3C (1C = 170 mAh g^{-1}). All cells were tested on LAND CT2001A battery tester. Electrochemical impedance spectroscopy was performed on a Reference 600 (Gamry Instruments) over a frequency range of 0.01 Hz to 1 MHz and the perturbation amplitude was 5 mV.

Computational Section: DFT modelling of IL decomposition was carried out using the Gaussian 16 package, according to methodology developed previously. Geometries of cations and anions, separately, were optimized using the M06-2X DFT functional and the 6–311++G(d,p) basis set. The effect of a liquid surrounding was modelled using the conductor-like polarizable continuum model (C-PCM) using parameters for water–as previously shown to be appropriate for highly polar solvents ($\varepsilon > 20$).[58] Reduction process at Li metal surface was simulated by introduction to the system an extra electron together with lithium cation. For cations, as reduced formed were found stable, breaking of all expected bonds was testing using energy scans, to find energy barriers (E_{akt}). Geometries of transition states were optimized and confirmed by presence of a negative frequency. Paths with the lowest E_{akt} were selected to follow to recombination products. Energy levels of the reaction steps were calculated based on the electronic energy, whereas reduction potentials (E_{red}) were determined using the thermodynamic cycle of the electrode reaction from Gibbs energies, as shown before.

Supporting Information

Supporting Information is available from the Wiley Online Library or from the author.

Conflict of Interest

The authors declare no conflict of interest.

[1] J. Janek, W. G. Zeier, *Nat. Energy* **2016**, *1*, 16141.

[2] K. Xu, *Chem. Rev.* **2014**, *114*, 11503.

[3] Z. Yu, D. G. Mackanic, W. Michaels, M. Lee, A. Pei, D. Feng, Q. Zhang, Y. Tsao, C. V. Amanchukwu, X. Yan, H. Wang, S. Chen, K. Liu, J. Kang, J. Qin, Y. Cui, Z. Bao, *Joule* **2019**, *3*, 2761.

[4] X. Xu, Z. Wen, X. Wu, X. Yang, Z. Gu, *J. Am. Ceram. Soc.* **2007**, *90*, 2802.

[5] J. Schnell, F. Tietz, C. Singer, A. Hofer, N. Billot, G. Reinhart, *Energy Environ. Sci.* **2019**, *12*, 1818.

[6] D. Lin, Y. Liu, Z. Liang, H. W. Lee, J. Sun, H. Wang, K. Yan, J. Xie, Y. Cui, *Nat. Nanotechnol.* **2016**, *11*, 626.

[7] A. Manthiram, X. Yu, S. Wang, *Nat. Rev. Mater.* **2017**, *2*, 16103.

[8] P. G. Bruce, A. R. West, *J. Electrochem. Soc.* **1983**, *130*, 662.

[9] R. Kanno, M. Murayama, *J. Electrochem. Soc.* **2001**, *148*, A742.

[10] H. Aono, *J. Electrochem. Soc.* **1993**, *140*, 1827.

[11] Y. Inaguma, C. Liquan, M. Itoh, T. Nakamura, T. Uchida, H. Ikuta, M. Wakihara, *Solid State Commun.* **1993**, *86*, 689.

[12] A. Emly, E. Kioupakis, A. Van der Ven, *Chem. Mater.* **2013**, *25*, 4663.

[13] X. Han, Y. Gong, K. K. Fu, X. He, G. T. Hitz, J. Dai, A. Pearse, B. Liu, H. Wang, G. Rubloff, Y. Mo, V. Thangadurai, E. D. Wachsman, L. Hu, *Nat. Mater.* **2017**, *16*, 572.

[14] F. Mizuno, A. Hayashi, K. Tadanaga, M. Tatsumisago, *Adv. Mater.* **2005**, *17*, 918.

[15] M. Matsuo, Y. Nakamori, S.-i. Orimo, H. Maekawa, H. Takamura, *Appl. Phys. Lett.* **2007**, *91*, 224103.

[16] J. Fu, *Solid State Ionics* **1997**, *104*, 191.

ADVANCED
SCIENCE NEWS
www.advancedsciencenews.com

ADVANCED
FUNCTIONAL
MATERIALS
www.afm-journal.de

[17] W. Liu, S. W. Lee, D. Lin, F. Shi, S. Wang, A. D. Sendek, Y. Cui, *Nat. Energy* **2017**, *2*, 17035.

[18] J. S. Thokchom, B. Kumar, *J. Power Sources* **2008**, *185*, 480.

[19] M. Guin, S. Indris, M. Kaus, H. Ehrenberg, F. Tietz, O. Guillon, *Solid State Ionics* **2017**, *302*, 102.

[20] Z. Sun, L. Liu, Y. Lu, G. Shi, J. Li, L. Ma, J. Zhao, H. An, *J. Eur. Ceram. Soc.* **2019**, *39*, 402.

[21] M. Du, K. Liao, Q. Lu, Z. Shao, *Energy Environ. Sci.* **2019**, *12*, 1780.

[22] P. Hartmann, T. Leichtweiss, M. R. Busche, M. Schneider, M. Reich, J. Sann, P. Adelhelm, J. Janek, *J. Phys. Chem. C* **2013**, *117*, 21064.

[23] J. A. Lewis, F. J. Q. Cortes, M. G. Boebinger, J. Tippens, T. S. Marchese, N. Kondekar, X. Liu, M. Chi, M. T. McDowell, *ACS Energy Lett.* **2019**, *4*, 591.

[24] H. Chung, B. Kang, *Chem. Mater.* **2017**, *29*, 8611.

[25] Y. Liu, C. Li, B. Li, H. Song, Z. Cheng, M. Chen, P. He, H. Zhou, *Adv. Energy Mater.* **2018**, *8*, 1702374.

[26] Q. Yu, D. Han, Q. Lu, Y. B. He, S. Li, Q. Liu, C. Han, F. Kang, B. Li, *ACS Appl. Mater. Interfaces* **2019**, *11*, 9911.

[27] Z. Zhang, S. Chen, J. Yang, G. Liu, X. Yao, P. Cui, X. Xu, *Electrochim. Acta* **2019**, *297*, 281.

[28] Z. Zhang, Y. Zhao, S. Chen, D. Xie, X. Yao, P. Cui, X. Xu, *J. Mater. Chem. A* **2017**, *5*, 16984.

[29] D. R. MacFarlane, M. Forsyth, P. C. Howlett, M. Kar, S. Passerini, J. M. Pringle, H. Ohno, M. Watanabe, F. Yan, W. Zheng, S. Zhang, J. Zhang, *Nat. Rev. Mater.* **2016**, *1*, 15005.

[30] D.-J. Yoo, K. J. Kim, J. W. Choi, *Adv. Energy Mater.* **2018**, *8*, 1702744.

[31] S. K. Singh, Shalu, L. B , H. Gupta, V. K. Singh, A. K. Tripathi, Y. L. Verma, R. K. Singh, *Energy* **2018**, *150*, 890.

[32] Q. Yang, Z. Zhang, X. G. Sun, Y. S. Hu, H. Xing, S. Dai, *Chem. Soc. Rev.* **2018**, *47*, 2020.

[33] I. A. Shkrob, T. W. Marin, Y. Zhu, D. P. Abraham, *J. Phys. Chem. C* **2014**, *118*, 19661.

[34] S. Xiong, K. Xie, E. Blomberg, P. Jacobsson, A. Matic, *J. Power Sources* **2014**, *252*, 150.

[35] B. V. Merinov, S. V. Zybin, S. Naserifar, S. Morozov, J. Oppenheim, W. A. Goddard, J. Lee, J. H. Lee, H. E. Han, Y. C. Choi, S. H. Kim, *J. Phys. Chem. Lett.* **2019**, *10*, 4577.

[36] Y. Lu, Z. Tu, L. A. Archer, *Nat. Mater.* **2014**, *13*, 961.

[37] P. Jankowski, N. Lindahl, J. Weidow, W. Wieczorek, P. Johansson, *ACS Appl. Energy Mater.* **2018**, *1*, 2582.

[38] H. Yildirim, J. B. Haskins, C. W. Bauschlicher, J. W. Lawson, *J. Phys. Chem. C* **2017**, *121*, 28214.

[39] A. J. Louli, L. D. Ellis, J. R. Dahn, *Joule* **2019**, *3*, 745.

[40] J. Nordström, L. Aguilera, A. Matic, *Langmuir* **2012**, *28*, 4080.

[41] B. Commarieu, A. Paolella, J.-C. Daigle, K. Zaghib, *Curr. Opin. Electrochem.* **2018**, *9*, 56.

[42] F. Sagane, T. Abe, Z. Ogumi, *J. Electrochem. Soc.* **2012**, *159*, A1766.

[43] M. R. Busche, T. Drossel, T. Leichtweiss, D. A. Weber, M. Falk, M. Schneider, M. L. Reich, H. Sommer, P. Adelhelm, J. Janek, *Nat. Chem.* **2016**, *8*, 426.

[44] X. He, P. W. Fuerschbach, T. DebRoy, *J. Phys. D: Appl. Phys.* **2003**, *36*, 1388.

[45] A. C. Ferrari, *Solid State Commun.* **2007**, *143*, 47.

[46] Q. Zhao, X. T. Liu, S. Stalin, K. Khan, L. A. Archer, *Nat. Energy* **2019**, *4*, 365.

[47] L. Porz, T. Swamy, B. W. Sheldon, D. Rettenwander, T. Frömling, H. L. Thaman, S. Berendts, R. Uecker, W. C. Carter, Y.-M. Chiang, *Adv. Energy Mater.* **2017**, *7*, 1701003.

[48] C.-Z. Zhao, P.-Y. Chen, R. Zhang, X. Chen, B.-Q. Li, X.-Q. Zhang, X.-B. Cheng, Q. Zhang, *Sci. Adv.* **2018**, *4*, eaat3446.

[49] C. Yang, H. Xie, W. Ping, K. Fu, B. Liu, J. Rao, J. Dai, C. Wang, G. Pastel, L. Hu, *Adv. Mater.* **2019**, *31*, 1804815.

[50] G. Hou, X. Ma, Q. Sun, Q. Ai, X. Xu, L. Chen, D. Li, J. Chen, H. Zhong, Y. Li, Z. Xu, P. Si, J. Feng, L. Zhang, F. Ding, L. Ci, *ACS Appl. Mater. Interfaces* **2018**, *10*, 18610.

[51] L. Liu, L. Chu, B. Jiang, M. Li, *Solid State Ionics* **2019**, *331*, 89.

[52] L. Yang, Z. Wang, Y. Feng, R. Tan, Y. Zuo, R. Gao, Y. Zhao, L. Han, Z. Wang, F. Pan, *Adv. Energy Mater.* **2017**, *7*, 1701437.

[53] Y.-C. Jung, M.-S. Park, C.-H. Doh, D.-W. Kim, *Electrochim. Acta* **2016**, *218*, 271.

[54] X. Wang, H. Zhai, B. Qie, Q. Cheng, A. Li, J. Borovilas, B. Xu, C. Shi, T. Jin, X. Liao, *Nano Energy* **2019**, *60*, 205.

[55] Q. Guo, Y. Han, H. Wang, S. Xiong, Y. Li, S. Liu, K. Xie, *ACS Appl. Mater. Interfaces* **2017**, *9*, 41837.

[56] Q. Cheng, A. Li, N. Li, S. Li, A. Zangiabadi, T.-D. Li, W. Huang, A. C. Li, T. Jin, Q. Song, W. Xu, N. Ni, H. Zhai, M. Dontigny, K. Zaghib, X. Chuan, D. Su, K. Yan, Y. Yang, *Joule* **2019**, *3*, 1510.

[57] S. Wang, J. Wang, J. Liu, H. Song, Y. Liu, P. Wang, P. He, J. Xu, H. Zhou, *J. Mater. Chem. A* **2018**, *6*, 21248.

[58] P. Jankowski, W. Wieczorek, P. Johansson, *J. Mol. Model.* **2017**, *23*, 6.